LANGMUIR

pubs.acs.org/Langmuir Article

Janus Particles with Flower-like Patches Prepared by Shadow Sphere Lithography

Layne Bradley,[‖] Xiangxin Lin,[‖] Yanjun Chen, Mona Asadinamin, Bin Ai,[*] and Yiping Zhao

Cite This: *Langmuir* 2021, 37, 13637−13644 Read Online

ACCESS | Metrics & More | Article Recommendations | Supporting Information

ABSTRACT: A general strategy for generating various Janus particles (JPs) based on shadow sphere lithography (SSL) by varying incident and azimuthal angles, as well as deposition numbers is introduced, forming well-identified flower-like patches on microsphere monolayers. An in-house simulation program is worked out to predict the patch morphology with complicated fabrication parameters. The predicted patch morphology matches quite well that of experimentally produced JPs. The relationships between patch shape/area/size/and incident angle/deposition numbers are quantitatively determined by calculating morphology and transmission spectrum correlations, which facilitated further implementation of SSL in fabricating more varieties of JPs. Such an SSL strategy can be used to create JPs with anticipated patch morphology and uniformity that may be used for self-assembly, drug delivery, or plasmonic sensors as well as exploring some fundamental principles relating to the properties of nanostructures.

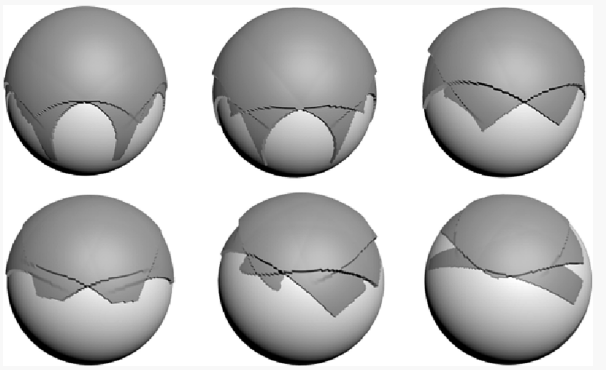

INTRODUCTION

Janus particles (JPs) have recently attracted a lot of research attention with various applications.[1] JPs, named after the Roman god Janus, are defined as colloidal particles of different sizes with more than one composition or chemical modification on different locations.[2,3] The functional patches with one or more different compositions on the JPs could have chemical properties that allow for the binding of complimentary nanoparticles or other specific molecules, they could have a magnetic property that allows for unique multiparticle assemblies[4] or external control,[5] or they could have an unique electromagnetic property useful for sensing[6] or probing the interactions of light and matter.[7] These JPs have demonstrated applications in interfacial stabilizers, catalysis, electrochemistry, biomedicine, etc.[8,9] All the properties and applications of JPs will depend on the morphology of Janus patches with defined size and chemical composition.

A variety of methods for creating JPs have been developed over the past few years to control their morphology and composition. Chemical methods such as surface nucleation and seeded growth can produce a large quantity of JPs at low cost.[10] The shape and size of JPs produced by these methods are hard to control, resulting in a decrease in uniformity. JPs can be produced at two-phase boundaries, but the fluctuations of interfaces and diffusion of modifying reagents limit the precise control of the modification area.[11,12] Electrochemical deposition can also produce large quantities of JPs with a precise two-phase boundary for a variety of materials.[13] The limitation is that the particles have to be made of conductive materials and that the deposited layer may have many defects or cracks.[14] In addition, JPs or multiphase particles can be synthesized by fluidic methods, such as microfluidic co-flow[15,16] and electrohydrodynamic co-jetting,[17,18] with good monodispersity and unique properties. However, those JPs are relatively large at around 100 μm in size with low yield. A more flexible and successful method to produce nanoscale JPs is shadow sphere lithography (SSL).[19,20] In SSL, the substrates with nanosphere/microsphere monolayers are placed within an evaporation chamber along with the source materials, but rather than having the face of the substrate perpendicular to the incoming deposition vapors, the substrate is tilted to an oblique angle. This tilting accentuates the shadowing effect of spheres on the substrate, creating a predictable morphology and shadowing environment. The SSL method has been studied to produce various patterns on substrates.[20,21] Dots,[22] triangles,[22] disks,[23] shells,[24] rods,[25] fan shapes,[26] Swiss rolls,[27] and many others have been fabricated on spheres by SSL, greatly expanding the variety and complexity of JPs. However, the studied JPs created by SSL are only the tip of the iceberg. As more varieties of JPs are fabricated by SSL, the full potential

Received: August 12, 2021
Revised: October 11, 2021
Published: October 18, 2021

https://doi.org/10.1021/acs.langmuir.1c02155
Langmuir 2021, 37, 13637−13644

of this process continues to expand. Establishing the relation between the patch morphology and fabrication parameters is a high priority, thus the desire to design and fabricate different kinds of JPs by SSL for various applications.

Here, JPs with flower-like patches are designed and prepared by SSL, revealing a general strategy of generating various JPs by varying incident and azimuthal angles as well as deposition numbers. A simulation program is worked out to predict the flower-like patch morphology with different fabrication parameters. Experimentally produced JPs by SSL show good agreement with the simulations. The uniformity of the fabricated patches at different monolayer domains at various fabrication parameters is discussed by calculating morphology and transmission spectrum correlations. The relationship between the patch morphology and fabrication parameters is established. Such a strategy can be used to create JPs with anticipated patch morphology and uniformity that may be used for self-assembly, drug delivery, or plasmonic sensors as well as exploring some fundamental principles relating to properties of nanostructures.

EXPERIMENTAL SECTION

Monolayer Fabrication. Monolayers of polystyrene (PS) spheres with diameter of 350 nm, 500 nm, 750 nm, 1 μm, and 2.0 μm were used for patch deposition to demonstrate the strategy to fabricate the JPs. The PS monolayers were formed using an air−water interface method described in a previous publication.[28] Glass and silicon substrates were cleaned with a piranha solution and rinsed with 18 MΩ water prior to being placed in the water below the floating monolayer. The water was gently removed, and the monolayer was then allowed to dry overnight on the substrates.

Fabrication of JPs. A home-built electron beam evaporation system was used to deposit Ag onto the monolayer substrates. The system was equipped with two stepper motors that controlled the polar rotation of the substrate to allow for changing the incident angle of the substrate as well as the azimuthal rotation of the substrates during deposition. The thickness and rate of Ag deposition was monitored by a quartz crystal microbalance (QCM). For all incident angle and rotation combinations discussed here, a total of 100 nm of Ag was deposited at a rate of 0.04 nm/sec.

Patch Morphology Simulation. A program developed in house was used to calculate and predict the resulting patches of the Ag depositions on the PS sphere monolayers.[26] This code takes into account the shadowing effect of the 36 nearest-neighbor nanospheres when calculating the deposition pattern. In order to simulate the effects of different monolayer domain orientations under different deposition conditions, multiple simulations were carried out by varying the initial domain orientation through a range of azimuthal angles from 0 to 55°. The program is shared at the website http://ailabcqu.com/GLAD?_l=en. The mechanism and user guide of the program are presented in the Supporting Information.

Patches obtained from MATLAB simulations were converted into binary matrices using image processing software (Image J, NIH). The MATLAB correlation function was then applied to these matrices to produce a Pearson correlation coefficient,[21,29] C_P, of the simulated patches at different azimuth angles, which quantifies the uniformity between the simulated patches.

Morphological and Optical Characterizations. The patch morphologies were characterized by a scanning electron microscopy (SEM, FEI Inspect F). Local experimental transmission $T(\lambda)$ and reflection $R(\lambda)$ spectra for each sample were measured by a custom spectroscopic microscope system with a spot size of 200 μm. Absorption spectra $A(\lambda)$ were calculated by $A(\lambda) = 1 - T(\lambda) - R(\lambda)$. The small focused spot size of the optical system allowed one to obtain the transmission measurement from a single domain at a time. For each sample, these local transmission spectra were recorded at nine distinct locations on the substrate. Effort was made so that each location was from a different domain when possible. The MATLAB correlation function was then applied to these spectra to produce the C_P, which quantifies the similarity between the experimental transmission spectra.

RESULTS AND DISCUSSION

The SSL deposition configuration is shown in Figure 1a. The PS sphere monolayer is in a closely packed hexagonal arrangement on a flat substrate. The parallel beam of deposition vapor flux comes to the substrate with an incident angle θ and an azimuthal angle φ, which can be varied. The θ is the angle between the vapor flux and the normal to the substrate surface, and φ is the azimuthal angle revolving the substrate plane. For a single deposition, both θ and φ are fixed. Multideposition can be performed with different θ and φ. The azimuthal rotation angle $\Delta\varphi$ between depositions is a function of n, the number of rotations, which is defined as $\Delta\varphi = 360°/n$.

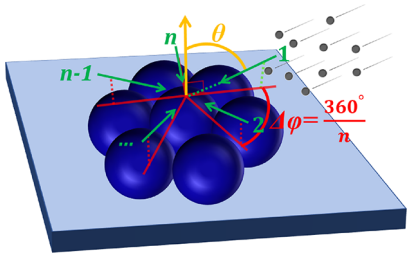

Figure 1. Schematic of the SSL deposition configuration on closely packed sphere monolayer substrates.

Through the in-house program, the patterns of deposited patches on the spheres were simulated for different numbers of rotations with a fixed $\theta = 75°$ and different initial azimuthal angle $\varphi_0 = 0$, 15, and 30°, respectively. The φ_0 is determined relative to the horizontal line between the centers of the adjacent spheres, as indicated in the first column of Figure 2. Since $\Delta\varphi = 360°/n$, at $n = 2$, 4, 5, 6, 7, and 8, $\Delta\varphi$ would be 180, 90, 72, 60, and 45°, respectively. The corresponding simulated patch patterns are shown in Figure 2. When $\varphi_0 = 0°$, the simulated patch morphology is as follows: When $n = 2$, a rectangular patch with a thin center and thick edge in the horizontal direction is formed on the sphere. When $n = 4$, the resulting patch has an octagon shape with a thin center and thick edge; with the increase of n, the shapes of the patches become more symmetric and flower-like with multiple "petals" deposited based on the main shadowing area. At $n = 5$ and 6, the patch clearly shows a flower shape with seven and six petals, respectively, where the center is thicker than the petals; when $n = 8$, the thick center is a clear hexagon, while the petal shows complicated shapes. Constant rotation or $\vec{n} \infty$ would lead to a spherical cap patch. The simulated patch morphology for different φ_o with the same n is compared: For small n ($\leq$ 4), since the patch shape is anisotropic, when φ_0 increases from 0−30°, the long axis of the patch patterns rotated with φ_0 while the shape also changes significantly. When $n = 2$, the shape changes from nearly rectangular at $\varphi_0 = 0°$ to quite obliquely tilted parallelograms at $\varphi_0 = 15$ and 30°; when $n = 4$, the shape at $\varphi_0 = 0°$ is quite different from the that at $\varphi_0 = 15°$, while similar with that at $\varphi_0 = 30°$ with a 30° rotation. For high-symmetry patches ($n > 5$), the orientation of the patch also rotates with φ_0, but the shape and overall area do not change significantly. With $n = 5$ and 6, the flower-like patches

https://doi.org/10.1021/acs.langmuir.1c02155
Langmuir 2021, 37, 13637−13644

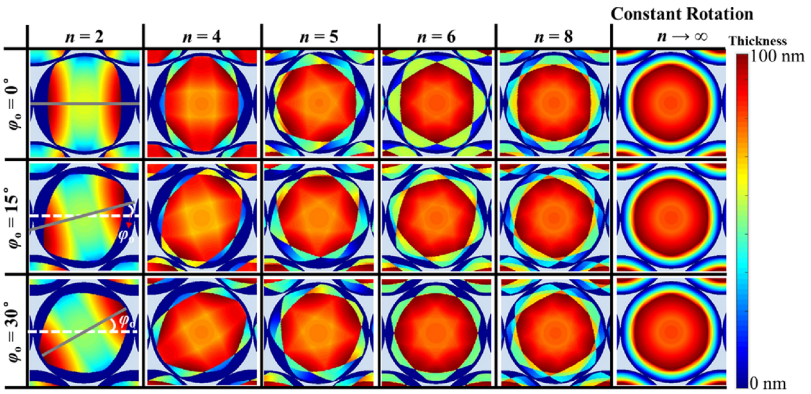

Figure 2. Simulated patch morphology on spheres for n = 2, 4, 5, 6, 8, and ∞ (constant rotation) with θ = 75° and the domains oriented at φ_o = 0, 15, and 30° which are indicated by the lines in the first column.

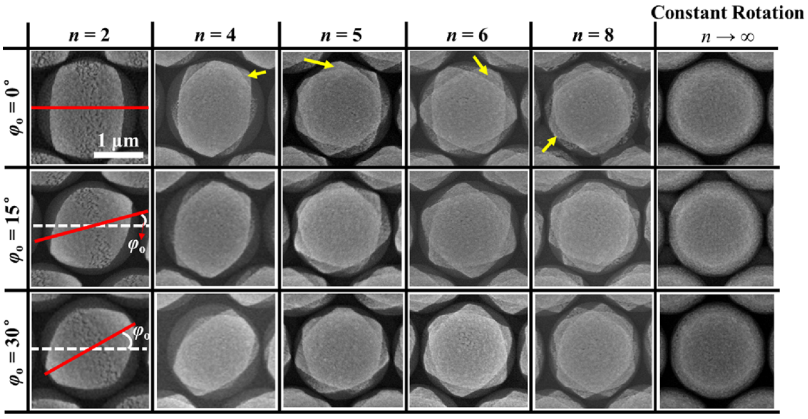

Figure 3. Representative SEM images of patches formed on 2 μm spheres from depositions performed at θ = 75°, n = 2, 4, 5, 6, 8, and ∞ (constant rotation), and φ_0 = 0, 15, and 30°, respectively. The red lines in the first column indicate the corresponding φ_0. The yellow arrows indicate the structural features. The scale bar is 1 μm and applies to all the SEM images.

all have seven and six distinct "petals" branching out from a central top, respectively; when n = 8, the patch shape remains similar, revolving with different φ_0. When the rotation is constant, i.e., $n \to \infty$, the patch keeps the same circular shape.

The corresponding experimental results for both n and φ_0 dependence are shown in Figure 3. The φ_0 is indicated by the angle between the red line and the horizontal white dotted line of the adjacent centers of two spheres, as shown in the first column of Figure 3. Overall, the patterns observed in experiment and those predicted by the program are in good agreement. More structural features (sharp tips and small gaps) appear when n increases from 2 to 8. The structural features are indicated by the arrows in Figure 3. As n continue to increase to ∞ (constant rotation), the patch would become a spherical cap (the rightest column in Figure 3), losing the sharp tips and small gaps. Electric field (E-field) can be significantly enhanced along the structural features, providing more hotspots for higher-performance plasmonic sensors and surface enhanced Raman scattering (SERS) substrates (Figure S3, SI). There are minute morphology differences on structural features such as tips and edges. Several reasons account for the difference observed in experiments. First, the simulation uses a deterministic model, in which no randomness or roughness has been taken into account, while the actual growth process is far from equilibrium and fluctuations in the deposition are unavoidable. Second, the simulation uses a continuum thin-film model, while in the experiment, many surface processes such as spontaneous adatom diffusion, desorption, and re-emission, in addition to the shadowing effect, could induce adatom clustering, re-evaporation, or capture at defect sites, which could significantly change the morphology of the patterns and introduce nonhomogeneous distribution of Ag.[21,26] Third, the shadow effect at each individual deposition is not counted in the simulation, while during the experiment, each deposition will create a thickness redistribution on each sphere which could induce changes in the final morphology. In addition, PS spheres with different diameters of 350 nm, 500 nm, 750 nm, 1 μm, and 2 μm were used for fabricating the patches. SEM images of patches on the 500 nm spheres are shown in Figure S4a,b in the SI. The patch morphology fabricated with the same fabrication parameters is the same, with the size simply scaled. SEM images of the 2 μm spheres are discussed because they are the clearest due to the large size. In addition, the JPs can be dispersed in solution and kept well-integrated (Figure S4c,d, SI).

Figure 4 shows the transmission, reflection, and absorption spectra of the patches on 500 nm spheres with different n. The optical properties of 500 nm JPs were studied because the main light-matter interaction was generated in the visible and near-infrared wavelength range, which is easy to test and used for more applications. The optical properties of the 2 μm JPs were also tested, as shown in Figure S5 in the SI. The light-matter interaction of the 2 μm JPs would be in the infrared wavelength range. No distinct peaks/dips can be observed in the visible and near-infrared wavelength range. For the transmission spectra in Figure 4a, the PS sphere monolayer

https://doi.org/10.1021/acs.langmuir.1c02155
Langmuir 2021, 37, 13637−13644

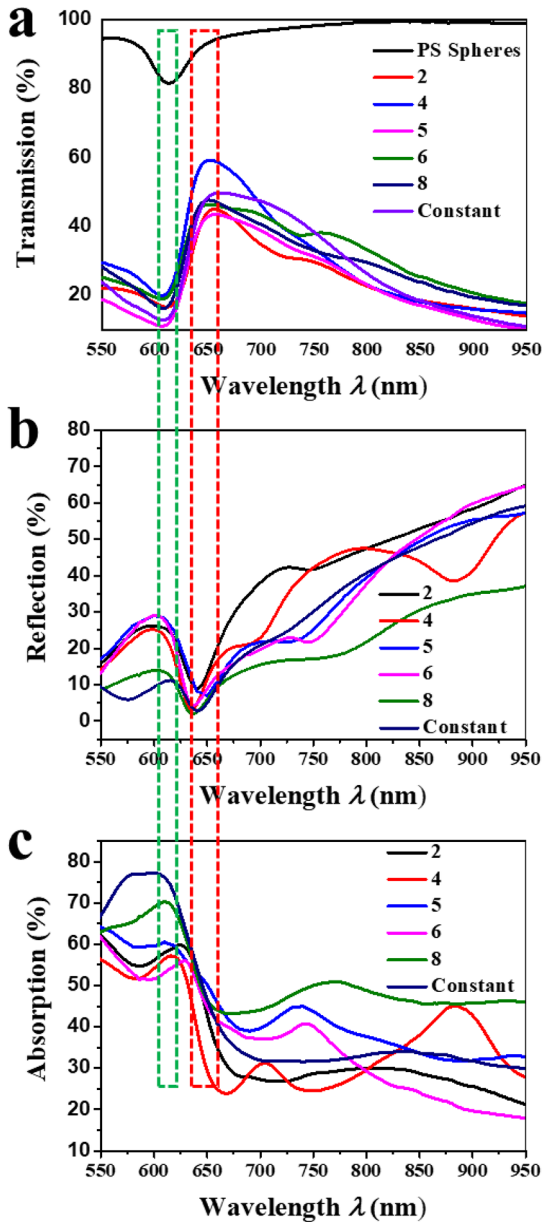

Figure 4. (a) Transmission, (b) reflection, and (c) absorption spectra of the patches on 500 nm spheres at $\theta = 75°$, $n = 2$, 4, 5, 6, 8, and ∞ (constant rotation). These spectra are averaged from nine domains. The green dotted rectangle indicates the photonic bandgap of the 500 nm sphere monolayer. The red dotted rectangle indicates the plasmonic resonances of the patches.

without patches shows a photonic bandgap at wavelength λ = ~610 nm. The photonic bandgap also appears in the transmission, reflection (Figure 4b), and absorption (Figure 4c) spectra of the patches, as indicated by the green dotted rectangle. The PS spheres with patches show distinct transmission peaks at λ = ~650 nm, which is attributed to the extraordinary optical transmission (EOT) phenomenon induced by plasmonic resonances of the Ag patches.[30,31] Correspondingly, the reflection spectra show dips at λ = ~650 nm as indicated in the red dotted rectangle. Overall, the spectral profiles of the patches are similar, while the intensity was varied for different patches but showed no obvious rules. Patches with different morphologies excite varied plasmonic resonances, showing the possibility of using patches to tune optical properties for specific applications. The effects of the different patches on the optical properties of the JPs are needed to be studied further by detailed calculation and experimental design.

The evolution of the patch area and shape can be characterized by a simple parameter, roundedness, which is defined as

$$R = \frac{1}{m}\sum_{m}\frac{s_i}{S} \tag{1}$$

where m is the number of radii points extracted from the circumference of the desired pattern and S is the maximum radius obtained from the circumference (or the radius of the sphere). S_i is the distance from the center to the ith radius point at the circumference. The roundedness R can be estimated numerically from both the SEM images (Figure 3) and simulated patterns (Figure 2) at different φ_0 (details can be seen in the SI). Figure 5a plots R versus n from both experimental data and simulation, where the R increases significantly from ~0.85 to ~0.95 with n. The R data are collected from 12 different φ_0 values (every 5° in the range of 0−55°). The increase in R means that the patch area becomes larger when more depositions (larger n) are performed. The error at each n is mostly smaller than 0.01, indicating that the patch area and shape are similar at different domains for a fixed n. Both R values from the experiments and the corresponding simulation are very close to each other. Overall, the R from the simulation is slightly larger than the R from experiments due to the increasing shadow effect in experimental deposition. In the simulation, the shadow effect at each individual deposition is not counted, i.e., the shadow effect is only determined by the sphere and does not change, while during the experiment, each deposition will create a thickness redistribution on each sphere

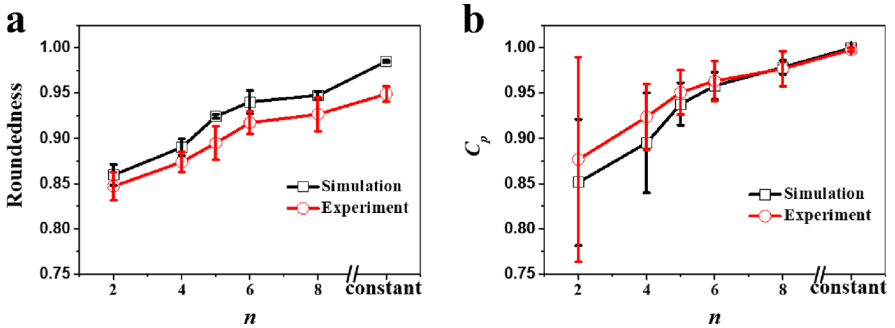

Figure 5. (a) The roundedness of the patch patterns versus n obtained experimentally and numerically. (b) The correlation coefficient C_P versus n, calculated between the transmission spectra and the simulated patterns.

https://doi.org/10.1021/acs.langmuir.1c02155
Langmuir 2021, 37, 13637−13644

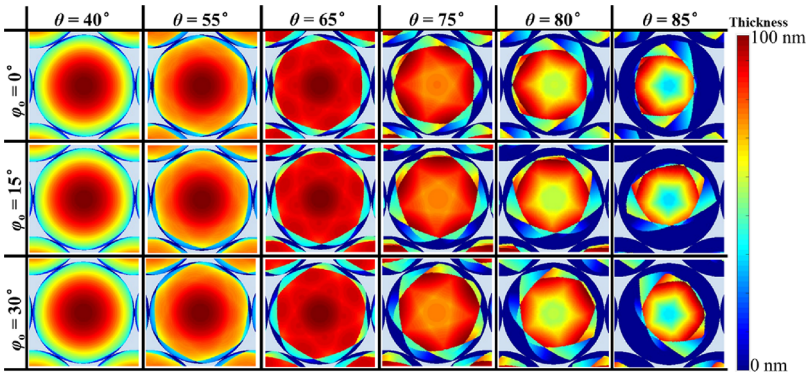

Figure 6. Simulated patch morphology on spheres for θ = 40, 55, 65, 75, 80, and 85°, respectively, with n = 5 at φ_0 = 0, 15, and 30°.

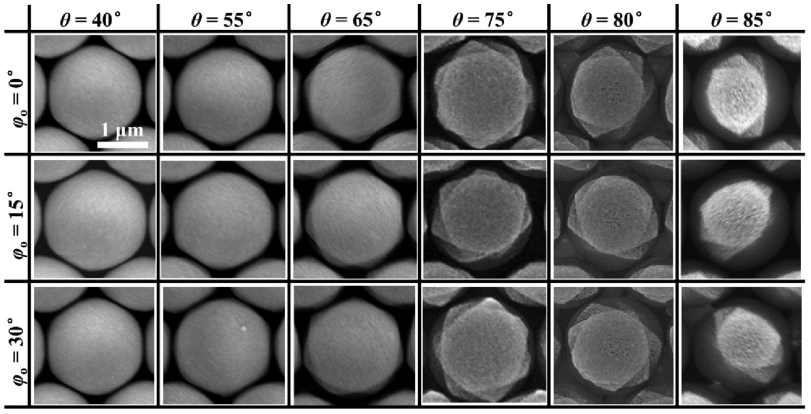

Figure 7. Representative SEM images of patches formed on 2 μm spheres for depositions performed at n = 5, θ = 40, 55, 65, 75, 80, and 85° and φ_0 = 0, 15, and 30°, respectively. The scale bar is 1 μm and applies to all the SEM images.

and increase the mask size; thus, the patch area (R) is smaller than that in the simulation. The uniformity of the patch shape is demonstrated by calculating the Pearson correlation coefficient C_P at different n and domains, as shown in Figure 5b. For the simulation (black dots and line), C_P is calculated from simulated images from the 2 μm spheres, showing a significant positive relationship with n. The error at each n shows a clear decreasing trend from 0.0697 to 0. These results indicate that more depositions lead to higher uniformity. For the experiment (red dots and line), C_P is calculated from the measured transmission spectra of patches on 500 nm spheres in order to statistically compare more patches and overall optical performance. Examples of the raw transmission spectra can be seen in Figure S7 in the SI. The C_P increase from ~0.87 to 1 and the error gradually vanishes with n, again revealing that high uniformity can be achieved by multiple depositions. The C_P from experiments is slightly larger than the corresponding C_P from the simulation because transmission spectra may be similar even with large morphology differences.

In order to further verify the effects of multiple depositions and create more patch morphologies, we repeated the n = 5 rotation prediction and experiments with different θ angles at θ = 40, 55, 65, 75, 80, and 85° as well as φ_0 = 0, 15, and 30°. Figure 6 shows the predicted results at different φ_0 (0, 15, and 30°, respectively). When θ = 40°, spherical cap patches with no distinct petals are formed; when θ = 55°, slightly polygonal shaped patterns are formed; when θ increases to 65°, seven small symmetric petals appeared. When θ increases further, the petal area and size keeps increasing while the symmetry starts to break. Compared to the patterns formed at θ = 65, 75, and 80°, the left petals are shorter than those of the right petals (φ_0 = 0°) while the top petals have the largest shape. When θ = 85°, a very anisotropic shape is formed. Also, similarly, for a fixed θ, when φ_0 is changing, the pattern starts to reorient according to φ_0.

Figure 7 shows SEM images of the corresponding deposited samples. Comparing Figure 7 with Figure 6, the experimental patterns and simulated patterns match quite well with each other. More structural features (sharp tips and small gaps) appear with increasing θ. The minute differences are due to the fluctuation and diffusion in the deposition process in the experiment. Figure 8 shows the transmission, reflection, and absorption spectra of the patches on 500 nm spheres with different θ. Clearly, in Figure 8a, the transmission spectra show the photonic bandgap of the 500 nm sphere monolayer at λ = ~610 nm and EOT peaks at λ = ~650 nm, whose effect can also be seen in the reflection (Figure 8b) and absorption (Figure 8c) spectra. The profiles of the transmission spectra for different θ are similar, while the transmission intensity generally increases with θ in a large range from ~5 to ~65% (as indicated by the red arrow in Figure 8a) because R (patch area) decreases from ~0.96 to ~0.79 (Figure 9a). In Figure 8b, the profile and intensity of the reflection spectra are similar, which may be due to the reflection being dominated by the scattering of the spheres and not the nanoscale structures. The absorption intensity included the effect of the transmission spectra, becoming smaller with θ from ~90 to ~20% as indicated by the red arrow in Figure 8c. The patch area played a major role in the optical properties, while the effect of the minute structures is not clear and needs to be further studied.

https://doi.org/10.1021/acs.langmuir.1c02155
Langmuir 2021, 37, 13637−13644

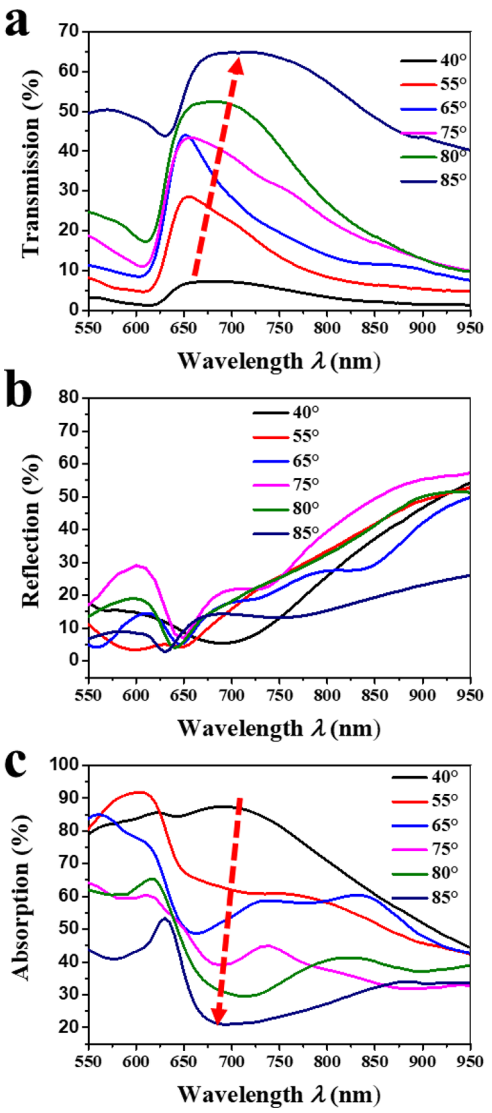

Figure 8. (a) Transmission, (b) reflection, and (c) absorption spectra of the patches on 500 nm spheres at n = 5 and θ = 40, 55, 65, 75, 80, and 85°. These spectra are averaged from nine domains. The red dotted line in (a) indicates that the transmission intensity increases with θ. The red dotted line in (c) indicates that the absorption intensity decreases with θ.

Overall, the distinct change of the transmission and absorption spectra is due to the large variations for the patch area, size, and shape, which again shows the great potential of the patches for light modulation.

The corresponding simulated and experimental roundedness R from different φ_0 are calculated and plotted as a function of θ in Figure 9a. The simulated and experimental R follow the same trend and decrease with θ, indicating that the patch area becomes smaller with θ, which is consistent with the fact that the patches become more anisotropic with θ as shown in Figure 7, and less surface of the sphere will be coated at larger θ. The error at each θ for the simulated patches is smaller than 0.007, indicating that the patch area and size are quite theoretically similar at different φ_0 for a fixed θ. The error at each θ for the experiments is also at a low level (0.007−0.02) but is slightly larger than that of the simulation. In addition, the experiment R is, in general, lower than that of the simulation. This difference is due to the fact that more variations, like shadow effect and vapor diffusion, would occur in the experiment. Figure 9b shows the plots of C_P from simulated images (from 2 μm spheres) and experimental transmission spectra (from 500 nm spheres) with different θ and domains. The raw transmission spectra are shown in Figure S8 in the SI. All of the C_Ps are larger than 0.97, and in general, they are nearly invariant with θ. This indicates that the uniformity of the patch is high and practically independent on θ when n = 5. In addition, the patches are also domain-independent at each θ since the errors in C_P are all very small (<0.01). Overall, according to both results by varying θ and n, we can come to following general conclusions: (1) A small θ angle and large n lead to a large patch area and high uniformity (domain-independent); (2) the number of structure features (sharp tips and small gaps that could serve as hotspots for E-field enhancement in plasmonics) is small when the θ is small (Figure 7), while the number of the structure features first increases and then decreases with n at large θ angle (Figure 3); and (3) to achieve high uniformity and more hotspots, the θ angle and n should be optimized to balance their positive and negative effects on the uniformity and number of hotspots.

CONCLUSIONS

Through engineering oblique angle depositions on colloidal monolayers, i.e., the so-called shadow sphere lithography, two sets of JPs with flower-like patches are fabricated by varying incident angles and azimuthal angles, respectively. The patch

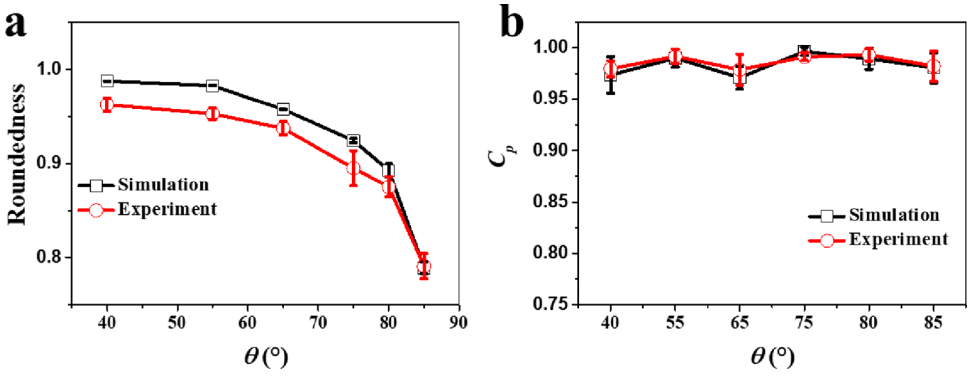

Figure 9. (a) Comparative roundedness of the depositions from the simulation and experiments with varying θ. (b) The C_P calculated from both the shape of the simulation from different domains as well as that calculated from the experimental transmission spectra at different locations with varying θ.

https://doi.org/10.1021/acs.langmuir.1c02155
Langmuir 2021, 37, 13637−13644

morphology can be well predicted by the in-house program and are consistent with the experimental results. The uniformity at different domains increases with increasing deposition number when the incident angle is fixed. The patch area and roundedness decrease with the increasing incident angle when the azimuthal angle is fixed. Essentially, JPs with numerous patch morphologies can be prepared by engineering a specific deposition number, incident angle, and azimuthal angle. The simulation and prediction of the patch morphology, as well as the quantitative study of uniformity and roundedness, will facilitate further implementation of SSL in fabricating more varieties of JPs. JPs with designed patch morphology and material can serve in applications of self-assembly, drug delivery, and plasmonic sensors as well as exploring some fundamental principles relating to properties of nanostructures.

■ ASSOCIATED CONTENT

Supporting Information

The Supporting Information is available free of charge at https://pubs.acs.org/doi/10.1021/acs.langmuir.1c02155.

Mechanism of the prediction program, user guide of the prediction program, FDTD calculation of *E*-field Distribution, SEM images of patches on 500 nm spheres, optical properties of patches on 2 μm spheres, calculation of roundedness, and transmission spectra (PDF)

■ AUTHOR INFORMATION

Corresponding Author

Bin Ai − *School of Microelectronics and Communication Engineering, Chongqing University, Chongqing 400044, P.R. China; Chongqing Key Laboratory of Bio-perception & Intelligent Information Processing, Chongqing 400044, P.R. China;* orcid.org/0000-0002-0502-9166; Email: binai@cqu.edu.cn

Authors

Layne Bradley − *Department of Physics and Astronomy, University of Georgia, Athens, Georgia 30602, United States*

Xiangxin Lin − *School of Microelectronics and Communication Engineering, Chongqing University, Chongqing 400044, P.R. China*

Yanjun Chen − *School of Microelectronics and Communication Engineering, Chongqing University, Chongqing 400044, P.R. China*

Mona Asadinamin − *Department of Physics and Astronomy, University of Georgia, Athens, Georgia 30602, United States*

Yiping Zhao − *Department of Physics and Astronomy, University of Georgia, Athens, Georgia 30602, United States;* orcid.org/0000-0002-3710-4159

Complete contact information is available at: https://pubs.acs.org/10.1021/acs.langmuir.1c02155

Author Contributions

‖L.B. and X.L. contributed equally to this work.

Author Contributions

L.B. and M.A. conducted the experiments. X.L. and Y.C. edited the program and performed the data analysis. B.A. and Y.Z. organized and wrote the manuscript. All authors contributed to the revision and final discussion of the manuscript.

Notes

The authors declare no competing financial interest.

■ ACKNOWLEDGMENTS

L.B., M.A., and Y.Z. were financially supported by the National Science Foundation under Grant No. ECCS-1808271. X.L., Y.C., and B.A. were partially supported by the Natural Science Foundation of Chongqing of China (cstc2020jcyj-msxmX0614), the Fundamental Research Funds for the Central Universities (2021CDJQY-010), Open Foundation of Defense Key Disciplines Lab of Novel Micro-Nano Devices and System Technology, and the Open Foundation of Chongqing University Key Lab of Optoelectronic Materials and Engineering.

■ REFERENCES

(1) de Gennes, P. G. Soft Matter. *Science* **1992**, *256*, 495.

(2) Yi, Y.; Sanchez, L.; Gao, Y.; Yu, Y. Janus Particles for Biological Imaging and Sensing. *Analyst* **2016**, *141*, 3526−3539.

(3) Walther, A.; Müller, A. H. E. Janus Particles: Synthesis, Self-Assembly, Physical Properties, and Applications. *Chem. Rev.* **2013**, *113*, 5194−5261.

(4) Yan, J.; Bloom, M.; Bae, S. C.; Luijten, E.; Granick, S. Linking Synchronization to Self-Assembly Using Magnetic Janus Colloids. *Nature* **2012**, *491*, 578−581.

(5) Jurado-Sanchez, B.; Pacheco, M.; Rojo, J.; Escarpa, A. Magnetocatalytic Graphene Quantum Dots Janus Micromotors for Bacterial Endotoxin Detection. *Angew. Chem., Int. Ed.* **2017**, *56*, 6957−6961.

(6) Zhang, Q.; Savagatrup, S.; Kaplonek, P.; Seeberger, P. H.; Swagert, T. M. Janus Emulsions for the Detection of Bacteria. *ACS Central Sci.* **2017**, *3*, 309−313.

(7) Schick, I.; Lorenz, S.; Gehrig, D.; Schilmann, A. M.; Bauer, H.; Panthofer, M.; Fischer, K.; Strand, D.; Laquai, F.; Tremel, W. Multifunctional Two-Photon Active Silica-Coated Au@Mno Janus Particles for Selective Dual Functionalization and Imaging. *J. Am. Chem. Soc.* **2014**, *136*, 2473−2483.

(8) Su, H.; Price, C. A. H.; Jing, L.; Tian, Q.; Liu, J.; Qian, K. Janus Particles: Design, Preparation, and Biomedical Applications. *Mater. Today Bio* **2019**, *4*, 100033.

(9) Zhang, J.; Grzybowski, B. A.; Granick, S. Janus Particle Synthesis, Assembly, and Application. *Langmuir* **2017**, *33*, 6964−6977.

(10) Wu, Z.; Li, L.; Liao, T.; Chen, X.; Jiang, W.; Luo, W.; Yang, J.; Sun, Z. Janus Nanoarchitectures: From Structural Design to Catalytic Applications. *Nano Today* **2018**, *22*, 62−82.

(11) Takahara, Y. K.; Ikeda, S.; Ishino, S.; Tachi, K.; Ikeue, K.; Sakata, T.; Hasegawa, T.; Mori, H.; Matsumura, M.; Ohtani, B. Asymmetrically Modified Silica Particles: A Simple Particulate Surfactant for Stabilization of Oil Droplets in Water. *J. Am. Chem. Soc.* **2005**, *127*, 6271−6275.

(12) Gu, H.; Yang, Z.; Gao, J.; Chang, C. K.; Xu, B. Heterodimers of Nanoparticles: Formation at a Liquid-Liquid Interface and Particle-Specific Surface Modification by Functional Molecules. *J. Am. Chem. Soc.* **2005**, *127*, 34−35.

(13) Loget, G.; Roche, J.; Gianessi, E.; Bouffier, L.; Kuhn, A. Indirect Bipolar Electrodeposition. *J. Am. Chem. Soc.* **2012**, *134*, 20033−20036.

(14) Wang, S.; Wu, N. Selecting the Swimming Mechanisms of Colloidal Particles: Bubble Propulsion Versus Self-Diffusiophoresis. *Langmuir* **2014**, *30*, 3477−3486.

(15) Nie, Z.; Li, W.; Seo, M.; Xu, S.; Kumacheva, E. Janus and Ternary Particles Generated by Microfluidic Synthesis: Design, Synthesis, and Self-Assembly. *J. Am. Chem. Soc.* **2006**, *128*, 9408−9412.

(16) Nisisako, T.; Torii, T.; Takahashi, T.; Takizawa, Y. Synthesis of Monodisperse Bicolored Janus Particles with Electrical Anisotropy Using a Microfluidic Co-Flow System. *Adv. Mater.* **2006**, *18*, 1152−1156.

(17) Roh, K. H.; Martin, D. C.; Lahann, J. Biphasic Janus Particles with Nanoscale Anisotropy. *Nat. Mater.* **2005**, *4*, 759−763.

(18) Lahann, J. Recent Progress in Nano-Biotechnology: Compartmentalized Micro- and Nanoparticles Via Electrohydrodynamic Co-Jetting. *Small* **2011**, *7*, 1149−1156.
(19) Ai, B.; Zhao, Y. Glancing Angle Deposition Meets Colloidal Lithography: A New Evolution in the design of Nanostructures. *NANO* **2018**, *8*, 1−26.
(20) Nemiroski, A.; Gonidec, M.; Fox, J. M.; Jean-Remy, P.; Turnage, E.; Whitesides, G. M. Engineering Shadows to Fabricate Optical Metasurfaces. *ACS Nano* **2014**, *8*, 11061−11070.
(21) Skehan, C.; Ai, B.; Larson, S. R.; Stone, K. M.; Dennis, W. M.; Zhao, Y. Plasmonic and Sers Performances of Compound Nanohole Arrays Fabricated by Shadow Sphere Lithography. *Nanotechnology* **2018**, *29*, No. 095301.
(22) Zhang, G.; Wang, D.; Möhwald, H. Nanoembossment of Au Patterns on Microspheres. *Chem. Mater.* **2006**, *18*, 3985−3992.
(23) Yu, Y.; Ai, B.; Möhwald, H.; Zhou, Z.; Zhang, G.; Yang, B. Fabrication of Binary and Ternary Hybrid Particles Based on Colloidal Lithography. *Chem. Mater.* **2012**, *24*, 4549−4555.
(24) Xie, D.; Hou, Y.; Su, Y.; Gao, F.; Du, J. Templated Fabrication of Hollow Nanospheres with 'Windows' of Accurate Size and Tunable Number. *Nanoscale Res. Lett.* **2015**, *10*, 153.
(25) Dolatshahi-Pirouz, A.; Sutherland, D. S.; Foss, M.; Besenbacher, F. Growth Characteristics of Inclined Columns Produced by Glancing Angle Deposition (Glad) and Colloidal Lithography. *Appl. Surf. Sci.* **2011**, *257*, 2226−2230.
(26) Larsen, G. K.; He, Y. Z.; Ingram, W.; Zhao, Y. P. Hidden Chirality in Superficially Racemic Patchy Silver Films. *Nano Lett.* **2013**, *13*, 6228−6232.
(27) He, Y.; Larsen, G.; Li, X.; Ingram, W.; Chen, F.; Zhao, Y. Nanoscale Conical Swiss Roll with Broadband Visible and Nir Circular Dichroism. *Adv. Opt. Mater.* **2015**, *3*, 342−346.
(28) Ingram, W. M.; Han, C.; Zhang, Q.; Zhao, Y. Optimization of Ag-Coated Polystyrene Nanosphere Substrates for Quantitative Surface-Enhanced Raman Spectroscopy Analysis. *J. Phys. Chem. C* **2015**, *119*, 27639−27648.
(29) Bradley, L.; Zhao, Y. Uniform Plasmonic Response of Colloidal Ag Patchy Particles Prepared by Swinging Oblique Angle Deposition. *Langmuir* **2016**, *32*, 4969−4974.
(30) Li, Y. Y.; Pan, J.; Zhan, P.; Zhu, S. N.; Ming, N. B.; Wang, Z. L.; Han, W. D.; Jiang, X. Y.; Zi, J. Surface Plasmon Coupling Enhanced Dielectric Environment Sensitivity in a Quasi-Three-Dimensional Metallic Nanohole Array. *Opt. Express* **2010**, *18*, 3546−3555.
(31) Ai, B.; Yu, Y.; Möhwald, H.; Zhang, G. Novel 3d Au Nanohole Arrays with Outstanding Optical Properties. *Nanotechnology* **2013**, *24*, No. 035303.

https://doi.org/10.1021/acs.langmuir.1c02155
Langmuir 2021, 37, 13637−13644